Diffraction-limited imaging with partially redundant masks: II. Optical imaging of faint sources

David F. Buscher

Naval Research Laboratory/U.S. Naval Observatory Optical Interferometer Project, U.S. Naval Observatory-AD5, 3450 Massachusetts Avenue, N.W., Washington, D.C. 20392-5420

Christopher A. Haniff*

Palomar Observatory, California Institute of Technology, Pasadena, California 91125

Received August 19, 1992; revised manuscript received March 23, 1993; accepted March 30, 1993

In a recent paper [J. Opt. Soc. Am. A **9**, 203 (1992)] the benefits of pupil apodization were examined for the near-infrared imaging of bright sources. In the current paper we extend these considerations to optical speckle imaging, in which photon noise rather than detector readout noise is important. We demonstrate that a one-dimensional pupil geometry (i.e., a thin slit) has several advantages over an unapodized aperture when faint sources are being observed through atmospheric turbulence. The use of a slit aperture does not decrease the signal-to-noise ratios of the power-spectrum and bispectrum measurements, and in many cases it increases them, despite the large reduction in signal level. The disadvantage of this apodization is a reduction in Fourier-plane coverage, which must be compensated for by observations with the slit aligned at several position angles. The performance of many of the current generation of photon-counting imaging detectors deteriorates at the high counting rates that can be experienced even when one is observing sources that are approaching the limiting magnitude of the speckle imaging technique. Under such conditions, we recommend the use of an apodized pupil, in contrast to the current preference for employing a neutral-density filter to reduce the detector count rate.

1. INTRODUCTION

Current high-resolution imaging experiments performed with astronomical telescopes almost exclusively use one of two diametrically opposed pupil geometries. At one extreme, in conventional speckle imaging,[1,2] the full telescope aperture is utilized to ensure that all spatial frequencies are measured simultaneously and to maximize the flux collected. In the past this type of approach has been adopted for numerous speckle observations of faint sources. At the other extreme, nonredundant masking techniques[3–5] employ screens located in the telescope pupil that pass light through a moderate number of appropriately arranged holes. Typically, the holes occupy a limited fraction of the total pupil area, and so only a small percentage of the flux intercepted by the telescope passes through to the detector. As a consequence, these methods are best suited for the observation of relatively bright sources, for example, supergiant stars.[6–8] The advantage of this approach is that the Fourier measurements from nonredundant masking observations are much less sensitive to the effects of turbulence-induced wave-front corrugations than those from fully filled-aperture methods.

In a previous paper,[9] hereafter referred to as paper I, we demonstrated that, at infrared wavelengths and in the presence of detector readout noise, there were compelling grounds for adopting a pupil geometry intermediate between the two extreme variants described above. We called these intermediate geometries partially redundant masks (PRM's). Our study showed that with use of a PRM (in this case a thin $\sim r_0$-wide annular aperture) in preference to the unapodized pupil, it was possible to increase the resistance of the observations to atmospheric wave-front fluctuations while still maintaining complete Fourier coverage and paying only a small penalty in limiting magnitude. In this paper we consider observations made at optical wavelengths at which the effects of the atmosphere are identical in nature but detector readout noise is negligible. In this regime our conclusions are somewhat different: an appropriately chosen partially redundant mask can yield Fourier measurements with better signal-to-noise ratios (SNR's) than provided by fully filled-aperture techniques when faint sources are being observed, at the expense of inferior Fourier-plane coverage.

Once again we find that the major advantage of using a PRM arises from practical considerations that are not normally taken into account in theoretical comparisons of imaging methodologies. We found that the most important reason for using a PRM at infrared wavelengths was the substantial improvement in Fourier-amplitude calibration under changing seeing conditions. We shall show that at optical wavelengths the use of a PRM is most advantageous in the large fraction of speckle observations in which the performance of a less-than-ideal photon-counting detector is the limiting factor in the experiment.

Our analysis and experimental results confirm and extend the results of Aime and Roddier[10] and of Kadiri *et al.*,[11] who analyzed a slit geometry in the context of speckle interferometry, using a one-dimensional scanning photomultiplier. We show that the slit geometry is still advantageous when considered in the context of modern two-dimensional detectors and when compared with a range of possible two-dimensional partially redundant pupil geometries. Furthermore, we have developed

0740-3232/93/091882-13$06.00

our treatment to include bispectrum analysis (in which the slit geometry is shown to be particularly advantageous) and two-dimensional image reconstruction in the presence of atmospheric turbulence.

We begin by examining the differences between optical and infrared speckle imaging, and in this context we define the imaging regime to be investigated in detail. Thereafter we follow an expository scheme similar to that employed in paper I, first using a heuristic model to explore qualitatively the space of possible pupil geometries (Section 3) and then examining selected geometries in greater detail, using a realistic numerical model of the atmospheric wave-front perturbations (Section 4). Up to this point, different pupil geometries will have been compared solely on the basis of pointwise SNR; in Section 5 we expand the discussion to include the imaging process as a whole. In Section 6 we present, as in paper I, experimental data that substantiate the conclusions of the previous analysis and demonstrate by way of image reconstructions the practicality of the technique for astronomical applications. Finally, in Section 7 we summarize our results and present our conclusions.

2. OPTICAL SPECKLE-IMAGING REGIME

We assume that the reader is familiar with the basic assumptions and nomenclature of our analysis of speckle imaging as applied in paper I. The two main differences between the near-infrared regime considered in that paper and the optical regime we are concerned with here are the scale sizes of the atmospheric wave-front perturbations and the detectors used.

The spatial and temporal scale sizes of the atmospheric seeing (r_0, the Fried parameter, and t_0, the coherence time) scale as $\lambda^{6/5}$. Thus the characteristic scales are of nearly a factor 6 smaller at $\lambda 0.5$ μm compared with their values at $\lambda 2.2$ μm. The difference in the value of r_0 means that an unapodized telescope is considerably more redundant at optical wavelengths than it is at infrared wavelengths; fortunately, this does not give rise to a substantial qualitative change in our analysis. Of greater importance is the reduction in the value of t_0: because exposure times at optical wavelengths must be correspondingly reduced (and also because photon-counting technology allows for more compact recording of each exposure), optical-speckle datasets typically consist of tens or hundreds of thousands of interferograms, compared with several hundred for a typical infrared-imaging experiment. This difference means that optical speckle observations are often made in a regime in which the SNR for a single exposure is small ($\ll 1$) but in which the average over a large number of exposures still can give an acceptable result. At these low light levels it is easy to show that the detector noise dominates the atmospheric noise, i.e., that the majority of the measurement noise is incurred in the detection of the interferogram rather than being due to fluctuations in the classical intensity distribution in the interferogram because of atmospheric seeing. Thus we shall for the most part neglect atmospheric noise in our discussion of optical imaging, in contrast to the discussion of paper I, in which atmospheric noise played a central role.

The other important difference between the optical and the near-infrared regimes concerns detector technology: most detectors used for infrared imaging are semiconductor devices that are limited by electronic readout noise; whereas, at optical wavelengths, photon-counting imaging devices are more often employed. Bare CCD's have been used successfully for optical-speckle imaging of relatively bright objects, but the readout noise and duty cycle of currently available devices make them less well suited for observations of faint objects. Thus the dominant source of detection noise at optical wavelengths is photon noise, which differs from readout noise in that it rises with increasing light level instead of being independent of it. We shall see later in the paper that this leads to a substantial change in the types of pupil geometry that are preferable: alarger apertures do not necessarily give better SNR's.

A more subtle difference between the detectors used in the two wavelength regimes is their linearity: typical near-infrared cameras operate linearly over a large range of incident flux levels, whereas the majority of optical photon-counting cameras suffer from significant nonlinearities, even for faint sources.

As an example, we can consider the PAPA camera[12]: at photon rates in excess of ~250,000/s the levels of artifacts introduced because of the limited response time of the event-registering electronics[13] rapidly become unacceptable. Typical limiting fluxes for other photon-counting cameras are even lower than this value (as shown, for example, by the experiments reported later in this paper). In comparison, very few images of astronomical objects have been reconstructed at photon rates of less than 0.1 photon per integration time per speckle; assuming that $r_0 = 10$ cm and $t_0 = 10$ ms, a photon rate of 0.1 photon/r_0^2/t_0 would lead to a total detected-photon rate of 160,000/s for a 4-m-diameter telescope. Thus, even in the faint source limit of the speckle-imaging technique, detector nonlinearities must be taken into account. All other things being equal, pupil geometries that reduce the effective photon flux and increase the rms speckle contrast are to be preferred: by this method the level of nonlinearities is decreased while the relative level of the speckle signal is boosted.

To summarize, we shall consider the optimization of the telescope pupil geometry in the photon-noise-limited regime but shall simultaneously be seeking geometries that minimize the effects of detector artifacts. As we have shown above, the regime in which both photon noise and detector nonlinearities are important covers most optical speckle-imaging observations of interest.

3. QUALITATIVE ANALYSIS

In this section and the next, we compare various pupil geometries purely on the basis of the pointwise SNR's of the power spectrum and the bispectrum measurements that they yield. Considerations such as Fourier coverage and resistance to detector artifacts will be deferred until Section 5.

A. Heuristic Model

As in paper I, we initially make use of a simplified atmospheric model in order to gain a broad understanding of the trade-offs involved in the selection of different pupil geometries. In this model the turbulent atmosphere is represented by a phase screen in front of the telescope that introduces random phase perturbations of many radians to

the incoming wave fronts. These perturbations are constant over areas (or subpupils) of dimension r_0 and are uncorrelated among subpupils. The temporal fluctuations are modeled by assuming that the phase screen is frozen during a time interval of length t_0 but that it changes randomly between successive coherence intervals. Following Readhead *et al.*,[14] we further simplify our representation by assuming that the coherent subpupils are square in shape and that the telescope primary mirror is also square.

B. Power-Spectrum Measurement

Since a speckle-imaging experiment can be considered to be an interferometric observation with redundant beam recombination, we can use Eq. (41) of Ref. 15 to compute the SNR of a power-spectrum measurement. For a pupil consisting of A subpupils and a baseline whose redundancy in the pupil is R, we have a SNR of

$$\mathrm{SNR}_{\mathrm{ps}} = \frac{N_0 R/A}{1 + N_0 R/A}, \tag{1}$$

where N_0 is the photon rate in photons per $r_0 \times r_0$ subpupil per integration time. For faint sources this reduces to

$$\mathrm{SNR}_{\mathrm{ps}} \approx N_0(R/A), \tag{2}$$

where we note that the result of this approximation is that the noise term resulting from atmospheric fluctuations has disappeared, leaving only the photon-noise term. A surprising feature of this equation is that the pupil area A enters in the denominator; more pupil area is not in general better. This is because the photon noise increases with the total number of collected photons. Larger pupils yield better SNR's only if they increase the redundancy R of a given baseline faster than the total pupil area increases.

With this in mind we can consider the sequence of pupil geometries shown in Fig. 1. Taking the nonredundant geometry [Fig. 1(a)] as a reference, we see first that geometries such as those shown in Fig. 1(b) that simply replicate the nonredundant aperture do not increase the SNR of the power-spectrum measurement on that baseline, since the pupil area increases in proportion to the baseline redundancy.

The annular geometry shown in Fig. 1(c) is even worse: nearly all baselines have a redundancy of only 2, whereas the area is much greater than that of the nonredundant pupil. Thus one of the properties of the annular geometry that was found to be advantageous in our study at near-infrared wavelengths, namely, its low redundancy, is found to be a disadvantage in this regime.

If we now consider the slit geometries shown in Figs. 1(d) and 1(e), we can see that these geometries do offer the prospect of increased SNR. Since the addition of only a single extra subpupil to the end of the slit increases the redundancy by unity [compared with two extra subpupils for the geometries shown in Figs. 1(a)–1(c)], slits of greater length yield better SNR's than do shorter slits, and an infinitely long slit has an R/A value of unity. If we augment the slit by increasing its width, by which we mean the dimension perpendicular to the direction of the baseline under consideration, as in Fig. 1(f), no improvement in the SNR is achieved, since the pupil area increases in direct proportion to the redundancy. It follows that the unapodized pupil, which is just a slit widened to its maximum extent, yields power-spectrum measurements with the same SNR as a slit of unit width and of length equal to the diameter of the telescope.

We should reiterate that here we are considering only the SNR of a single power-spectrum component; we consider the consequences of the greater number of power-spectrum components measured by the unapodized pupil in Section 5.

C. Bispectrum Measurement

Instead of using the phase error to parameterize the accuracy of the bispectrum measurements, as in paper I, we use its inverse here, the phase SNR:

$$\mathrm{SNR}_{\mathrm{bs}} \equiv \frac{|\langle S \rangle|}{\sigma_\perp}, \tag{3}$$

where $\sigma_\perp{}^2$ is the variance of the complex bispectrum phasor in the direction perpendicular to the mean phasor and $\langle S \rangle$ is the mean phasor. The main reason for making this change is so that subsequent plots of three-dimensional surfaces showing bispectrum accuracy versus coordinate will show the areas of highest accuracy as peaks instead of being hidden in valleys.

To evaluate the phase SNR for our simplified atmospheric model, we make use of the work of Readhead *et al.*,[14] who show that the mean amplitude of a given bispectrum component increases linearly with the triplet redundancy of the component in the pupil. The term triplet redundancy refers to the number of subpupil triplets in the telescope pupil that measure the three Fourier components, $\mathbf{u}_1$, $\mathbf{u}_2$, and $\mathbf{u}_1 + \mathbf{u}_2$, that give rise to the bispectrum coordinate $(\mathbf{u}_1, \mathbf{u}_2)$. This definition of redundancy in terms of subpupil triplets rather than baseline triplets is important, because it automatically excludes nonclosing triplets of baselines that do not contribute to the mean bispectrum amplitude in the presence of wave-front perturbations. The variance of the bispectrum caused by photon noise is in general a complicated function of the detected-photon rate,[2] but at low light levels the rms noise becomes equal to $N^{3/2}/\sqrt{2}$, where N is the total number of photons detected per integration. Under these conditions the noise

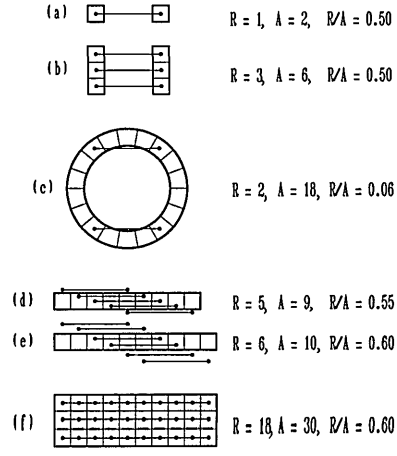

Fig. 1. Schematic diagrams of various pupil geometries. The redundant copies of a given baseline are represented by the dumbell-shaped diagrams. The values of the baseline redundancy R and the pupil area A are given beside each pupil.

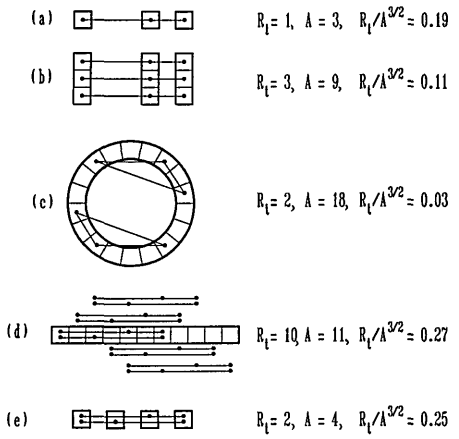

Fig. 2. Schematic diagrams of various pupil geometries. The redundant copies of a given pupil triplet are represented by the triple-dumbell diagrams. The values of the triplet redundancy R_t and the pupil area A are given beside each pupil.

is symmetric in the complex plane, and the phase SNR is given by

$$\mathrm{SNR}_{\mathrm{bs}} = \frac{N_0{}^3 R_t}{(N_0 A)^{3/2}/\sqrt{2}} = \sqrt{2} N_0{}^{3/2}\left(\frac{R_t}{A^{3/2}}\right), \tag{4}$$

where R_t is the triplet redundancy of the given bispectrum component and the other terms are as defined previously. Note that a comparison of Eqs. (2) and (4) reveals that the SNR penalty induced by an increase in the pupil area is more severe for the bispectrum than for the power spectrum.

The consequences of this property are illustrated when we consider a set of pupils similar to those examined in the previous subsection but modified so that the simplest nonredundant configuration has three apertures instead of two (Fig. 2). This figure differs from Fig. 1 in showing schematically the triplet redundancy instead of the baseline redundancy of each pupil. When one is considering the bispectrum SNR, changes in geometry that increase the redundancy in proportion to the pupil area, such as going from Fig. 2(a) to Fig. 2(b), are actually detrimental: the value of R_t/A is constant, but the value of $R_t/A^{3/2}$ decreases.

The annular geometry [Fig. 2(c)] illustrates two further points. First, this pupil does not measure the same bispectrum triangles as do the more linear pupil geometries, despite having complete Fourier coverage. Thus a direct comparison of the SNR of the same bispectrum point is impossible. The second point is that the redundancy of those bispectrum triangles that are measured by this aperture is only 2, and so the SNR properties of this pupil are as poor in the bispectrum domain as they are in the power-spectrum domain.

A slit pupil [Fig. 2(d)] offers much better performance; in fact it gains an increase in triplet redundancy of 2 for each unit increase in length, because symmetric triplets in the pupil contribute to the same bispectrum component. For very long slits, however, the increase in redundancy is directly proportional to the pupil area, and so, as seen above, this results in a net decrease in SNR. Thus for any given bispectrum component there will be an optimal slit length that maximizes the SNR of that particular measurement. By differentiating an expression for the ratio $R_t/A^{3/2}$ as a function of the slit length, we can show that a (linear) bispectrum component whose maximum baseline is B has maximum SNR for a slit of length $3B$.

It is easy to see that wider slits, and by extension unapodized apertures, have worse bispectrum SNR properties than the corresponding unit-width slits, since the ratio R_t/A will be constant but A will be increasing.

We leave it as a heuristic exercise for the reader to convince herself or himself that no other qualitatively different geometries offer significantly better performance. One interesting geometry is that shown in Fig. 2(e), which capitalizes on the redundancy increase offered by addition of a symmetric triplet to the pupil. It can be shown, however, that an optimal slit pupil yields a greater SNR if the maximum baseline of the bispectrum component being considered satisfies $B < 10r_0$. Furthermore, we shall see in Section 4 that a more realistic atmospheric model favors continuous apertures that exploit the medium-scale correlations in the atmospheric wave-front perturbations that are known to exist.

4. NUMERICAL SIMULATIONS

A. Numerical Procedure

While the previous heuristic analysis is important in defining the relative importance of various features of partially redundant pupil geometries in terms of the noise on power-spectrum and bispectrum measurements, it can provide only qualitative insights. In this section we use the results from numerical simulations based on a more realistic atmospheric model to derive more accurate quantitative results.

In the simulations, we employed numerically generated wave-front perturbations with a Kolmogorov spectrum so as to treat properly the spatial statistics of the atmospheric fluctuations. The simulation process was very similar to that used in paper I, and the reader is directed there for a detailed description. We simulated the process of imaging through turbulence by generating a randomly perturbed wave front on a numerical grid, multiplying it by the appropriate pupil function, and Fourier transforming it to obtain a simulated image (or specklegram) of a point source as seen through the telescope–atmosphere combination. The temporal evolution of the wave fronts was modeled very coarsely: the wave fronts were assumed to remain frozen during the exposure time of each specklegram, a new wave front being generated for successive exposures. From a large number of these simulated specklegrams (for the simulations discussed here, typically 10^5 were generated per pupil configuration) the ensemble average of any property of a speckle image could be determined.

For photon-noise-limited measurements, the variances of the power spectrum and the bispectrum can be derived with two different methods. The first is similar to that used in paper I, in which analytical expressions for the noise as a function of light level were employed, the simulated high-light-level specklegrams being used to determine the mean values of the Fourier quantities appearing in the formulas. We have used this method here for investigating the power-spectral SNR. Unfortunately, problems can arise when one is attempting to utilize this approach for determining the noise on the bispectrum, be-

cause the analytical formula is rather long[2,16]: in certain circumstances as many as 70 terms need to be considered for adequate accuracy to be maintained. In such cases we have used a more direct route to determine the noise. Poisson-limited versions of the specklegrams were generated at various photon rates, and the noise was estimated directly from the ensemble variances of the measured bispectrum. This method has the advantage of simplicity but is more computationally intensive, since a new ensemble of specklegrams has to be prepared for determining the noise at each light level of interest.

In all the simulations described below, the wave fronts were generated on a uniform grid with ≥ 5 samples per r_0. For the purposes of illustration, we chose to examine the following telescope pupil geometries: (a) the full pupil, here taken to be an unobstructed circular aperture of diameter $D = 25.6r_0$; this corresponds to interferograms obtained on a 4-m telescope at a wavelength of 750 nm in 1-arcsec seeing, (b) an annular aperture with inner diameter $23.6r_0$ and width $1r_0$, and (c) slit geometries in which the long dimension was held constant at $25.6r_0$ and the short dimension was varied from $0.5r_0$ to $16r_0$. The ends of the slits were rounded so as to take account of the circular telescope aperture.

B. Power-Spectrum Measurements

1. *Signal-to-Noise Ratio*

It is well established[17,18] that in the presence of photon and atmospheric noise the SNR for power-spectrum measurements can be written as

$$\mathrm{SNR}_{\mathrm{ps}} = \frac{\bar{N}\langle I^{(2)}(\mathbf{u})\rangle}{[1 + 2\bar{N}\langle I^{(2)}(\mathbf{u})\rangle + \bar{N}^2\,\mathrm{var}\{I^{(2)}(\mathbf{u})\} + \langle I^{(2)}(2\mathbf{u})\rangle]^{1/2}}, \tag{5}$$

where $\bar{N}$ is the mean number of photon counts detected per interferogram and $I^{(2)}(\mathbf{u})$ is the value of the high-light-level image power spectrum at spatial frequency $\mathbf{u}$, the spectrum being normalized so as to have unit value at the origin. Angle brackets ($\langle Q\rangle$) denote the ensemble average of a quantity Q, while $\mathrm{var}\{Q\}$ denotes its variance.

We have used this formula and the mean values of the high-light-level quantities from simulations to derive the SNR for the pupil geometries discussed above. The results have been evaluated assuming an unresolved source and that $N_0 = 0.1$, i.e., for a detected-photon rate of 0.1 photons per coherence area per coherence time, and are plotted in Fig. 3(a). In the interests of clarity, in this and certain subsequent plots the results for slit pupils appreciably wider than $4r_0$ have not been displayed. For such wide slits the behavior of the power-spectrum and bispectrum SNR tends asymptotically toward that of the filled pupil and so is not particularly revealing. Because the photon rate has been parameterized in terms of the number of photons detected per r_0-sized patch, it is important to recognize that the total number of photons detected per interferogram is not constant but varies from 3 for the narrowest slit-shaped pupil, through 10 for the annular pupil, to 66 for the filled aperture.

As expected, these data show that there is little or no advantage, in terms of enhanced power-spectrum SNR, in using a filled pupil instead of a narrow slit. Indeed, at the higher spatial frequencies, beyond ~3/4 of the telescope cutoff frequency, the slit-type pupil geometries provide a higher SNR despite their smaller effective areas. We can explain this in terms of pupil redundancies: the redundancy of a circular pupil tapers off more rapidly than a slit at high spatial frequencies. The only region in which the most redundant pupil is favored is at spatial frequencies less than r_0/λ. This so-called seeing spike is a result of short-range correlations in the wave front on scales of order r_0, but it is of little interest for high-spatial-resolution observations.

Figure 3(a) also confirms the inferior performance of an annular pupil in this regime: the power-spectrum SNR is more than a factor of 10 lower than that offered by the other pupil geometries for essentially all spatial frequencies. As mentioned in Subsection 2.B, this aspect of the thin annular pupil arises because of its low redundancy but large area, features that, interestingly, become advantageous at infrared wavelengths.

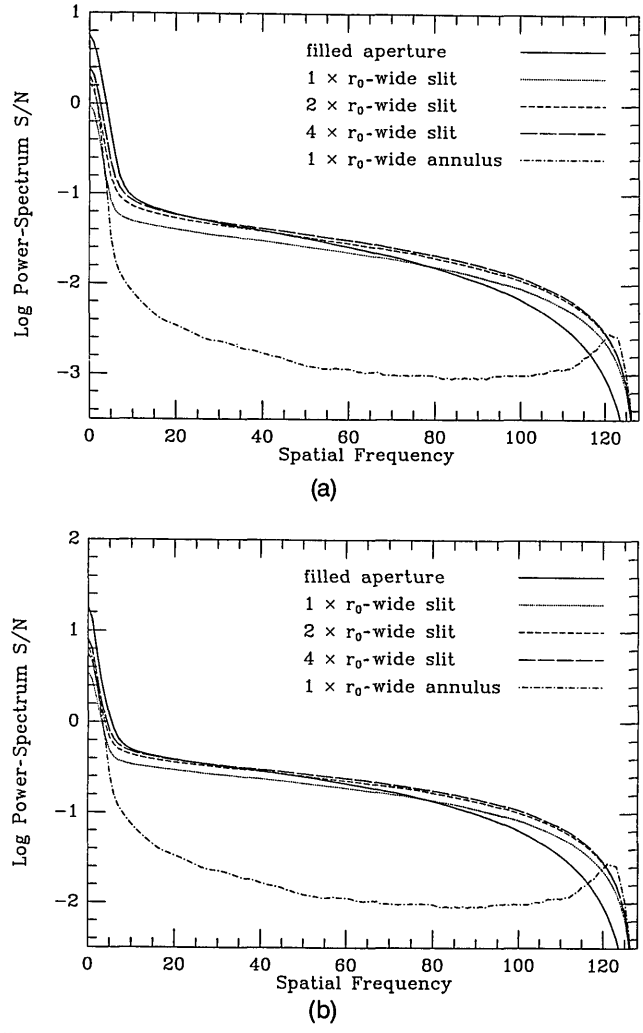

Fig. 3. Power-spectrum SNR as a function of spatial frequency for a variety of pupil geometries. The curves in (a) have been evaluated for a photon rate of 0.1 photon per r_0-sized patch per coherent integration time, while those in (b) have been computed for a photon rate ten times higher. The SNR is relatively independent of the total number of photons detected for the slit and for the fully filled pupil, and at high spatial frequencies the pupils with smaller area give the best SNR's. The seeing limit (r_0/λ) corresponds to a spatial frequency of 5 units, and the diffraction limit to 128 units.

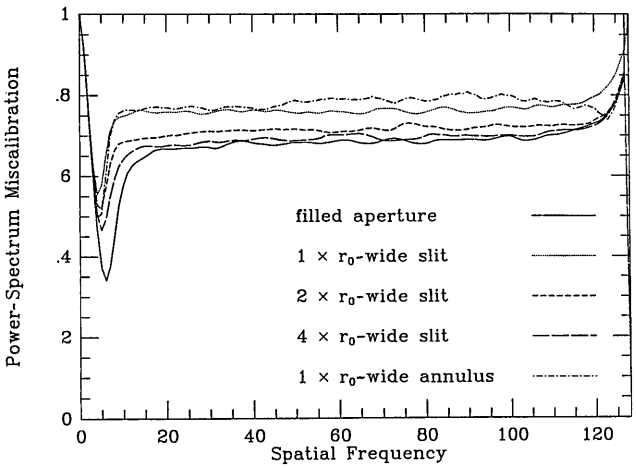

Fig. 4. Fractional miscalibration of the mean power spectrum when the Fried parameter r_0 rises by 20% between the observations of source and calibrator. Curves are plotted for the filled aperture, a thin annular pupil, and three of the slit-type pupils discussed in the text.

At higher light levels these conclusions are hardly altered. Figure 3(b) shows similar curves evaluated for a photon rate 10 times higher. Apart from an overall increase in the SNR that applies to all the functions plotted, the relative differences between the alternative pupil geometries are almost unchanged.

2. *Amplitude Calibration*

As well as affecting the SNR's of power-spectrum measurements, the pupil geometry also can modify the sensitivity of these measurements to fluctuations in the mean seeing parameters. Following paper I, we have investigated this by computing the calibration errors that would have occurred had the value of r_0 increased by 20% between the observation of the source of interest and its calibration source. These results are shown in Fig. 4, where we have plotted the fractional error of the power spectrum as a function of spatial frequency for the pupils discussed above. Over most of the spatial-frequency range there is little to choose between the wider slits and the filled aperture, with the calibration error remaining constant at ~30%. The only region in which the lower redundancy of the slit apertures becomes noticeable is within the seeing spike, where the effects are localized over a small range of spatial frequencies. The $1 \times r_0$-wide slit and the annular pupil perform somewhat better, giving fractional miscalibrations of ~20% in the high-frequency regime.

In comparison with our investigation at near-infrared wavelengths, pupil apodization is less advantageous in the optical regime, because the miscalibration curve for the unapodized pupil is much flatter than its infrared counterpart (see paper I, Fig. 5). This can be explained in terms of the much lower ratio of D/r_0 at infrared wavelengths: miscalibration effects associated with the region near the seeing spike and near the diffraction-limit cutoff occupy proportionately less of the available spatial-frequency space in the optical case. Furthermore, the preferred partially redundant pupil geometries at optical wavelengths have much higher redundancies than their infrared counterparts and thus can offer less in terms of resistance to miscalibration.

C. Bispectrum Measurements

As discussed in Subsection 4.A, we have computed the bispectrum-phase SNR's for several pupil geometries, using the variances derived explicitly from ensembles of simulated Poisson-limited specklegrams. We have already demonstrated that the Fourier data obtained with an annular pupil will have SNR's that are much inferior to those of the other pupil geometries that we have examined, and therefore we have not included an annular pupil configuration for these simulations. For the purposes of comparison between the unapodized and the slit-type pupils, the most useful portion of the bispectrum lies in a two-dimensional subplane of the bispectral 4-space. We shall hereafter plot bispectral functions in a rectangular (u_1, u_2) coordinate system, where u_1 and u_2 are the moduli of the spatial frequencies $\mathbf{u}_1$ and $\mathbf{u}_2$, which are aligned with the long axis of the slit. In this representation the support of the bispectrum is a hexagon, but because of the symmetries of the bispectrum, the nondegenerate portion of this support is contained in a triangle bounded by the lines $u_1 = 0$, $u_1 = u_2$, and $u_1 + u_2 = u_{\max}$, where $u_{\max}$ is the maximum spatial frequency sampled by the aperture.

Figure 5 shows a surface plot of the bispectral-phase SNR computed for a filled telescope aperture and a detected-photon rate of 0.1 photon per r_0-sized patch. In this and subsequent plots three distinct regions can be identified:

1. The region near the origin, of highest SNR, that corresponds to the bispectral seeing spike: $\{u_1, u_2\} \lesssim r_0/\lambda$.
2. A region of moderate SNR lying next to the u_1 axis: $u_1 \gtrsim r_0/\lambda$, $u_2 \lesssim r_0/\lambda$. By analogy with the seeing spike familiar from speckle power-spectrum analyses, this region can be thought of as a bispectral seeing ridge and is sometimes called the near-axis region.
3. A gently sloping plateau region in which the SNR is typically much lower than in the other two regions: $\{u_1, u_2\} \gtrsim r_0/\lambda$.

We should note that the existence of regions 1 and 2 was not revealed in the heuristic study presented earlier in Section 3. The seeing spike and ridge are produced by the short-range correlations in the atmospherically perturbed wave fronts, which were not taken into account in the discretized model that we used. However, our previous discussion does explain why region 3 has such a low SNR, especially in the case of the filled pupil, and this insight will be useful later on in the paper.

In order to assess the relative information contents of these three regions, we need to consider both the magnitude of the SNR and the Fourier-plane requirements of the particular imaging program being undertaken. Within region 1, all the spatial frequencies contributing to the bispectrum are less than or comparable with the seeing limit, and so this zone is relatively unimportant for high-resolution imaging. On the other hand, region 3 contains only high-spatial-frequency information and has by far the largest area, but its SNR is low. As a result, most of the data in this region are never used in speckle-imaging studies, because the number of independent interferograms recorded is usually too few to permit the phase error of the averaged bispectrum to be reduced to less than

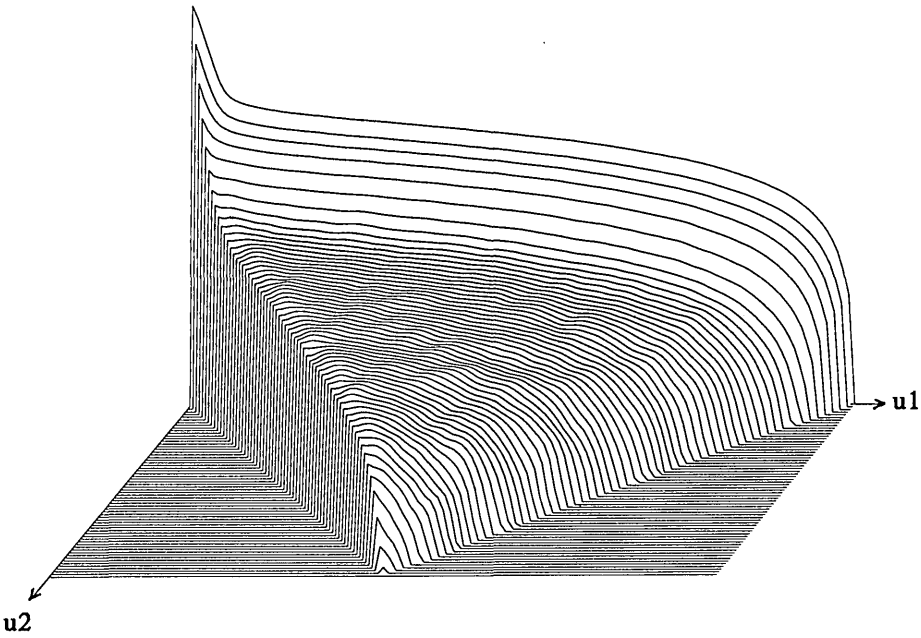

Fig. 5. Three-dimensional surface plot of the bispectrum-phase SNR for the filled pupil, evaluated for a photon rate of 0.1 detected photon per coherence patch per coherence time. Only the nondegenerate portion of the bispectrum, which has a triangular support in the (u_1, u_2) plane, is plotted. The vertical height of the surface at any point is proportional to the logarithm of the phase SNR at that point.

a few radians. Region 2 is thus the most useful for obtaining images with resolutions exceeding the seeing limit.

The competition between SNR and sensitivity to high-spatial-frequency information that is evident in the comparison of regions 1–3 is itself mirrored within region 2. Here the bispectral components with highest SNR lie close to the u_1 axis (see Fig. 5). However, these data are less sensitive to small-scale object structure than to corresponding points far away from the u_1 axis. This can be illustrated in an extreme manner by considering the line in the bispectrum defined by $u_2 = 0$. Along this line the SNR of a bispectrum-phase measurement is in fact infinite, since the bispectrum here is a simple multiple of the power spectrum, $I(0)I(u_1)I(-u_1)$. However, despite this perfect measurement of the bispectrum phase, this part of the bispectrum is of no use in determining the object phase, because we know *a priori* that the phase of the power spectrum is zero. This asymptotic result also applies in a modified form to other areas within region 2. By considering a simple case such as a close binary star,[19] we can show that the sensitivity of the bispectrum phase to small-scale object structure increases with distance from the u_1 axis. We can understand this statement from another point of view by considering the reconstruction of the object Fourier phase with use of a recursive phase-retrieval technique.[20] Many more steps of recursion and hence much more bispectrum data will be needed if we use only bispectrum points lying close to the u_1 axis.

For the purposes of expediency we shall hereafter adopt a coarse approximation and assume that the information content per unit bispectrum area is uniform within the seeing ridge and zero outside it. In addition we shall define the outer boundary of the seeing ridge as the locus of points beyond which the SNR of the bispectrum is so low that, even after being averaged over a large number of interferograms, the bispectrum phase cannot be measured to better than 1 rad. Because the typical number of interferograms collected in a speckle-imaging experiment is in the range 10^4–10^6, this definition implies that the seeing ridge will be bounded by a contour at a level of the order of 10^{-2}–10^{-3} in the bispectral SNR.

With this definition in mind, we are now in a position to compare the bispectrum properties of our different pupil geometries. If we consider first the regions bounded by the 10^{-2} contours in the six individual panels of Fig. 6 (which correspond to a photon rate of 0.1 photon per coherence patch per exposure), it is evident that there are only small differences among the various pupils despite the widely differing numbers of photons collected by each of them: in all cases these contours bound a region roughly r_0/λ wide running along the u_1 axis. The contours extend to slightly higher u_1 values for the slits than for the filled aperture, with the maximum extent occurring for the $4r_0$-wide slit. If we now consider the 10^{-3} contours in the same figures, a somewhat different picture appears. The regions bounded by these contours occupy a substantial fraction of the bispectrum plane for the narrow slits but contract in size as the total pupil area increases. For the filled pupil, the region bounded by the 10^{-3} contour is not much larger than that bounded by the 10^{-2} contour. Consequently the bispectrum data obtained with the slit pupils constrain much more strongly the small-scale object structure than do the equivalent data measured when the full aperture is used. A comparison of Figs. 6(a)–6(f) indicates that the extent of the regions bounded by the 10^{-3} contours begins to reduce significantly for slit widths greater than $4r_0$. Since the $4r_0$ aperture shows the greatest extension for the region bounded by the 10^{-2} contour, we can identify this aperture as offering the best overall performance in terms of bispectrum-phase sensitivity.

The dependence of the bispectrum SNR on the pupil redundancy can be explained heuristically as follows: the

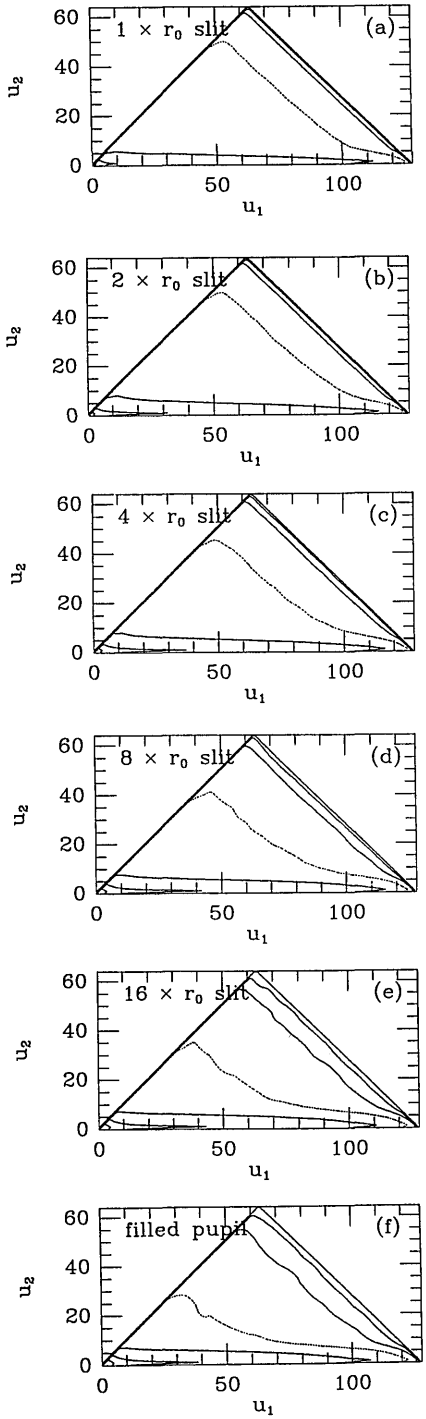

Fig. 6. Contour plots of the bispectrum-phase SNR for five slit pupils and a filled aperture. All the slits have a long dimension that is equal to the diameter of the filled aperture ($25.6r_0$) and short dimensions of r_0, $2r_0$, $4r_0$, $8r_0$, and $16r_0$. The simulated photon rate is 0.1 photon per coherence patch per coherence time, i.e., the mean photon rates per interferogram are 3, 7, 13, 26, 49, and 66 for (a), (b), (c), (d), (e), and (f), respectively. The contour levels are plotted at values of 10^{-9}, 10^{-5}, 10^{-4}, 10^{-3}, 10^{-2}, 10^{-1}, and 10^{0}. For clarity the 10^{-3} levels are shown as dotted curves. The seeing limit corresponds to a spatial frequency of 5 units.

SNR in the near-axis region follows closely the value of the power-spectral SNR.[2] As we have seen, the power-spectrum SNR is slightly better for the slit pupils, and so these pupils give rise to less-noisy data in the equivalent regions of the near-axis bispectrum. As we descend to the 10^{-3} contour, we begin to include parts of the plateau region, which our heuristic analysis showed had a higher SNR for pupils with low-to-moderate redundancy. Thus a contour of fixed height will enclose a substantial fraction of the available bispectrum in the case of a slit pupil while extending only a short distance from the u_1 axis in the case of the filled aperture.

At higher photon rates (Figs. 7 and 8) our conclusions are similar, although the discussion pertaining to the 10^{-3} contour now applies to the 10^{-2} and the 10^{-1} contour. In practice, the contour actually chosen to delimit the usable area of the bispectrum will depend on the details of the particular observation. For example, if a heavily resolved object is being observed, then all the contours will shift inward toward the u_1 axis. Nevertheless, whichever contour is chosen to delimit the usable bispectrum, it will encompass a larger area when data are collected with a slit pupil than when data are obtained with the filled aperture.

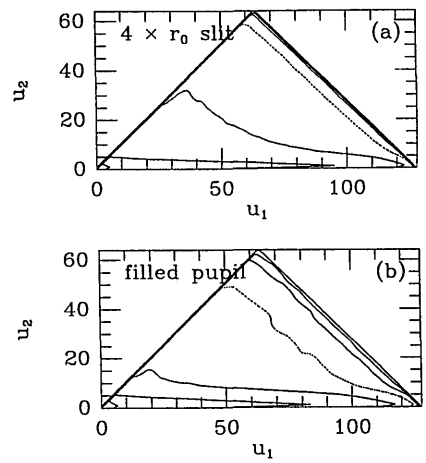

Fig. 7. Contour plots of the bispectrum-phase SNR for (a) the $4r_0$-wide slit and (b) the filled aperture. The simulated photon rate is 0.3 photon per r_0-sized patch per coherent integration time, i.e., 3 times the rate used to generate Fig. 6. The contour levels are the same as for Fig. 6.

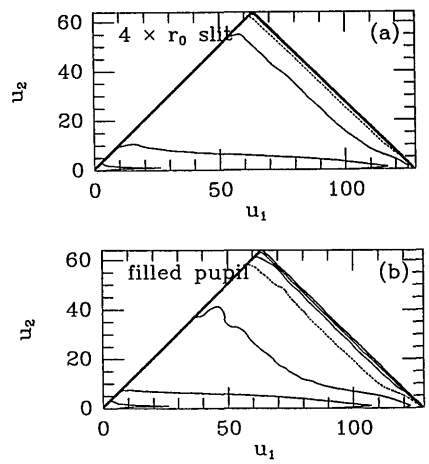

Fig. 8. Contour plots of the bispectrum-phase SNR for (a) the $4r_0$-wide slit and (b) the filled aperture. The simulated photon rate is 1.0 photon per r_0-sized patch per coherent integration time, i.e., 10 times the rate used to generate Fig. 6. The contour levels are the same as for Figs. 6 and 7.

5. PARTIALLY REDUNDANT MASKS IN PRACTICAL IMAGING SITUATIONS

In the previous sections we have demonstrated that slit pupils have properties that are equivalent or superior to those of unapodized apertures, when a pointwise comparison of their Fourier-plane SNR's is made. We have repeatedly emphasized that this is only a partial measure of their efficacy in high-resolution imaging; two additional repercussions of pupil apodization that must be taken into account are Fourier-plane coverage and the effects of detector nonlinearities.

The Fourier-plane coverage of a slit aperture is effectively one dimensional, whereas the unapodized pupil measures spatial frequencies over a circular region. In order to make two-dimensional images with a slit pupil, one must collect data with the slit located at several different position angles with respect to the source. The number of position angles that are necessary will depend on the complexity of the source being imaged. Experience in radio astronomy has shown that the number of Fourier-plane data required for successful image synthesis is of the order of the number of filled resolution elements in the image. With the exception of solar system objects, most targets of speckle-imaging programs have been relatively simple. Thus a moderate number of position angles, of the order of 10, probably would suffice in most cases but at a substantial cost in terms of extra observing time in comparison with the filled pupil. This cost can be partly offset because the slit masks provide data of higher SNR, which reduces the amount of observing time required per position angle. Indeed, the experimental data presented later in the paper show that in practical situations the SNR increase offered by a slit pupil can be so large as to result in a net decrease in observing time.

We note that there are circumstances in which the extra Fourier coverage afforded by a filled pupil is of no benefit.[21] For example, there are considerable astrophysical advantages to observing in multiple wave bands simultaneously.[22] For this spectral information to be obtained, a broad-band speckle pattern must be spectrally dispersed. High-spatial-frequency information in one dimension is thereby smeared out, leading to one-dimensional Fourier coverage independent of the pupil geometry.

When detector nonlinearities are significant, and we have shown in Section 2 that this can occur even for speckle imaging of faint objects, it is clear that the use of a slit mask offers substantial advantages. In contrast to the traditional practice of using a neutral-density filter to limit the photon rate to an acceptable level, the introduction of a slit mask into the pupil allows the count rate to be reduced substantially without sacrificing sensitivity. This reduction can result in a substantial saving of observing time, since the number of exposures required for attaining a given final SNR increases as the square of the attenuation of the neutral-density filter.

Furthermore, the use of a slit mask increases the contrast of the speckle pattern: this is the reason that SNR is relatively high in comparison with the photon rate.[11] Thus the relative effect of detector nonlinearities is less for an experiment that uses the slit geometry even when compared with the effect in an experiment performed at the same photon rate with a filled aperture in combination with a neutral-density filter.

A third benefit of using a slit mask in the presence of detector artifacts arises paradoxically from the limited spatial-frequency coverage that we previously considered a disadvantage. Compensation of detector nonlinearities[18,23,24] usually cannot be accomplished analytically but instead involves fitting some empirical function in the spatial-frequency domain over the region where it is known *a priori* that there is no signal power, i.e., beyond the diffraction limit of the telescope. The results are then interpolated to the spatial frequencies that contain useful data, and the compensation is applied. As with nonredundant masks, the use of a slit pupil ensures that the regions containing signal power in the Fourier plane are relatively small so that both the fitting and subsequent interpolation can be performed straightforwardly. In contrast, in the case of the fully filled aperture, the regions available for characterizing the Fourier-plane artifacts will be much smaller. Furthermore, the fitted function must be interpolated over the whole of the central region of the Fourier plane, a procedure that is considerably less robust. Thus in cases in which it is important to characterize both the detector and the source under study, the use of an apodizing mask permits a useful compromise to be made in terms of the spatial frequencies separately allocated for these two purposes.

We can summarize the theoretical analyses of the preceding sections as follows: (1) as far as pointwise comparisons are concerned, the slit aperture has somewhat better SNR characteristics than an unapodized aperture; (2) when Fourier-plane coverage is taken into account, an unapodized aperture may be preferable when the object of interest is very complex or for the very faintest sources when observing time is at a premium; (3) when detector artifacts are the limiting factor in data quality, a slit aperture is to be preferred. Unfortunately, it is difficult to define at what point the crossover between these two (i.e., observing-time and detector-artifact-limited) regimes occurs from a theoretical standpoint alone, since it will depend strongly on the details of the individual detector and of the observation being performed. This problem is better addressed, if only partially, by experiment.

6. OBSERVATIONAL RESULTS

Although our analytic and numerical results are of interest from a purely academic point of view and highlight many of the attractive features of partially redundant pupil geometries, a persuasive case for their adoption must rest on whether they can be utilized for the high-resolution imaging of faint astronomical sources. With this in mind we performed two preliminary experiments, using the Hale 5-m telescope at Palomar Observatory during the fall of 1991 to assess the feasibility of using slit-type pupil masks for low-light-level speckle observations.

A. Fourier-Plane Signal-to-Noise Measurements

The initial observations were aimed solely at verification of our numerical results. Point-source speckle data were secured at the *f*/415 Gregorian focus of the 5-m telescope during the night of September 29, 1991, with a Ranicon photon-counting camera. We used a 7.5-nm FWHM interference filter centered on 701 nm to define the optical bandpass, and for technical reasons we stopped the tele-

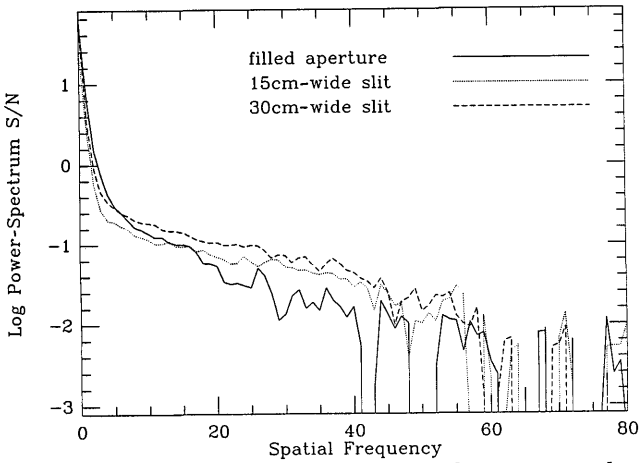

Fig. 9. Observed power-spectrum SNR per frame measured at the Hale 5-m telescope. The effective photon rates were 10, 20, and 265 per interferogram for the three pupil geometries investigated. A spatial frequency of 80 corresponds to the maximum observed baseline of 4.5 m. Note the better SNR characteristics of the pupils with smaller effective area.

scope down to 4.45 m. More complete details of the speckle camera and the observational setup can be found elsewhere.[7,25] Data were obtained with the unapodized 4.45-m pupil and through two linear pupil-plane masks of dimensions 4 m × 10 cm and 4 m × 20 cm. The detected-photon rate from the source, SAO 53264, was 0.20/10 ms per 10-cm-diameter patch of pupil, which gave photon rates of 10, 20, and 265 per 10 ms for the differing pupil configurations. The FWHM of long-exposure images were ~0.8 arcsec.

In Fig. 9 we show the mean power-spectrum SNR as a function of spatial frequency for the filled aperture and for the two linear pupils. For baselines longer than ~3 m, the data from all three pupils are too poor, because of the low light level and the limited number of specklegrams, to permit reliable Fourier-amplitude determination. These results are in good qualitative agreement with our predictions, with the filled aperture providing the data of lowest SNR and the wider of the slits offering the highest-quality data. However, in a quantitative sense there are discrepancies between these results and our predictions. First, the SNR's obtained with all the pupils are generally lower than expected from our simulations. This is understandable, given the fact that our numerical model did not include the effects of telescope aberrations, finite optical bandwidth, and finite exposure time, all of which would be expected to lower the amplitude of the high-spatial-frequency Fourier components. A second discrepancy is that the relative superiority of the slit apertures over the filled pupil is in fact greater in magnitude than predicted. One reason for this is that the telescope suffers from a small amount of astigmatism: using only a restricted region of the full pupil reduces the effects of this additional phase perturbation. A second explanation for the better relative performance of the slit geometries is the photon camera itself. Even at the low photon rates experienced here, the effects of saturation in the microchannel pores of the photon-counting camera are important. This saturation manifests itself as a reduction in the SNR at moderate and high spatial frequencies. These data thus provide a good example of a situation in which the use of a pupil-plane mask is positively advantageous *because* it limits the flux from the source.

Our results for the bispectrum are displayed in Fig. 10. In each panel we have plotted a gray-scale representation of the bispectrum-phase SNR ratio over the two-dimensional subplane of the bispectrum sampled by the linear pupils. The gray scale is chosen so that regions appearing white have SNR's, after averaging 15,500 interferograms, of less than 2. In practice, regions of such low SNR's are rarely used for Fourier-phase recovery, so that the total gray area in each figure can be used as a measure of the amount of useful information contained in the data. The utility of the partially redundant pupils is self-evident, with the pupils of lower redundancy providing bispectrum-phase measurements of higher SNR. As above, the effects of detector nonlinearities at high counting rates serve only to accentuate the limitations of the filled aperture, and it is clear that the 20-cm-slit pupil offers the best all-around performance in terms of providing a much larger number of usable bispectrum phases despite its reduced area when compared with the filled aperture.

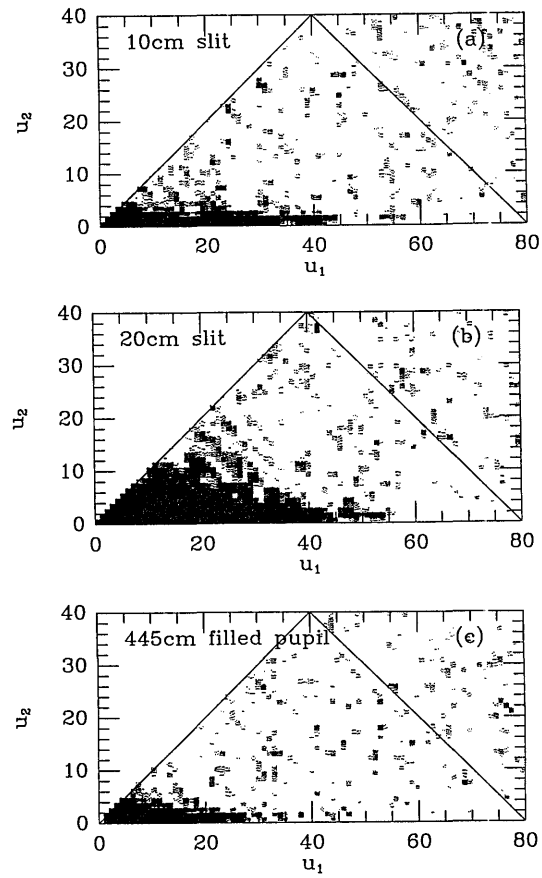

Fig. 10. Observed bispectrum-phase SNR measured at the Hale 5-m telescope. The effective photon rates were 10, 20, and 256 per interferogram for the three pupil geometries investigated. The gray scale runs logarithmically from −0.1 to 7.9, i.e., white regions of the plot contain no useful signal because the SNR after averaging 15,500 frames is less than 2 [$\log(\sqrt{15{,}500}) = 2.1$]. The triangular contour defines the support of the nondegenerate portion of the bispectrum sampled by the telescope. The regions beyond this that appear to contain signal correspond to spatial frequencies sampled by the detector but not by the telescope. As in Fig. 9, a spatial frequency of 80 corresponds to a baseline of 4.5 m.

B. Two-Dimensional Imaging

Although the use of one-dimensional telescope pupils was studied extensively in the late 1970's and early 1980's in the context of high-resolution imaging,[26–28] these treatments did not address the problem of image reconstruction in the presence of turbulence. To examine the imaging potential of slit-type pupil geometries, observations of the 0.5-arcsec binary star ϕ Andromedae were made on the night of September 28, 1991. These utilized a 4 m × 10 cm pupil mask and the same detector and filter used for the point-source observations described above. Between 2 and 3 min of data were collected, with the mask located at six position angles with respect to the source so that the visibility function of the source and that of its calibrator, SAO 37375, could be sampled adequately. A neutral-density filter also was used to limit the photon rate to 2.0/10 ms per 10-cm-diameter patch of pupil. In fact, because of the relatively poor seeing at the time, the data were analyzed with an exposure time of 5 ms so as to maximize the SNR of the averaged power spectra and bispectra. This gave a photon rate of 50 per interferogram for the source and 160 per interferogram for the calibrator star.

In principle, the reconstruction of diffraction-limited images from sequences of interferograms obtained through a one-dimensional pupil is straightforward. For each set of data, collected with the pupil aligned at some position angle with respect to the source, the power spectrum and the bispectrum of the source and the calibrator are accumulated. These averaged quantities can then be calibrated against each other and the source Fourier amplitudes and phases extracted by use of standard methods. Image reconstruction from such data can be accomplished by means of several routes. One method, perhaps the most familiar to the optical-signal-processing community, would be to recover the Fourier phases from the bispectrum by either a recursive or a least-squares procedure, combine these data with the measured Fourier amplitudes, and then perform an inverse Fourier transform to produce a one-dimensional profile of the source brightness distribution. This procedure would be repeated for all mask position angles, a final two-dimensional image being recovered from the projections by means of standard tomographic reconstruction techniques.

Following paper I, we have chosen to use an alternative technique developed in radio astronomy. This so-called self-calibration technique[29] combines the phase-retrieval and the tomographic-inversion steps into a single iterative algorithm. This technique permits a more realistic treatment of noise as well as permitting the incorporation of image-plane constraints (e.g., positivity and extent) throughout all steps of the image restoration. In order to utilize standard radio astronomy software, we have sampled the Fourier plane at a set of discrete locations corresponding to some particular interferometric array, i.e., a so-called pseudoarray. The power spectrum and the bispectrum are subsequently accumulated at only this small set of points, the Fourier data thereafter being treated as though they actually had been collected with such a pseudoarray. Further details of the basis and the rationale for such an approach can be found elsewhere.[30,31]

Images recovered from our sparsely sampled power-spectrum and bispectrum estimates are shown in Figs. 11(a) and 11(b). We used a six-element pseudoarray with a maximum baseline of 2.2 m, which gave a total of 90 visibility amplitudes and 120 bispectrum phases for the complete set of data. For the second of the reconstructions, we simulated even lower-light-level observations (25 photons per 5-ms interferogram) by using a software filter that discarded every other photon in the analysis. In both images the binary companion is clearly visible: 0.49 arcsec from the primary in position angle 130°. At the higher photon rate [Fig. 11(a)], the quality of the reconstruction is very good: the dynamic range of the image, as determined by the ratio of the peak brightness to the

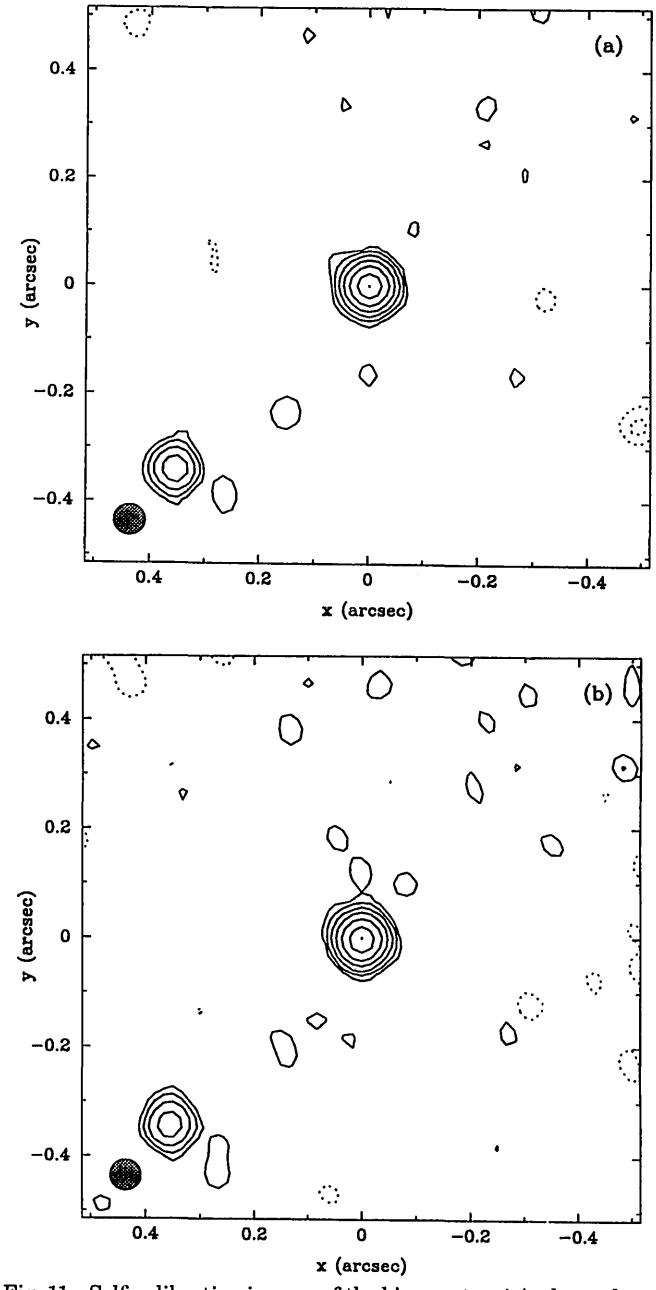

Fig. 11 Self-calibration images of the binary star ϕ Andromedae obtained with a 4 m × 10 cm pupil mask. Contours are plotted at −2, 2, 4, 8, 16, 32, 64, and 99% of the peak intensity. The effective photon rates were (a) 50 and (b) 25 per interferogram. The restoring beam for each image is shown in the lower left-hand corner. North is up, and East is to the left.

brightness of the weakest believable feature in the map, is ~50:1, and most of the field is free of artifacts. The map reconstructed at lower light levels is somewhat noisier. There are an increased number of noise spikes distributed across the map plane, the binary companion appears slightly misshapen, and the dynamic range is lower. Nevertheless, the separation, position angle, and flux of the companion agree well with the values determined from the higher-quality image, and in this respect the reconstruction remains reliable. In comparison with other speckle-interferometric image reconstructions made at similar light levels and of equivalent resolution,[25] these preliminary images are of excellent quality.

7. SUMMARY

We have demonstrated that the pupil geometry should be considered an important parameter in the design of a speckle-imaging experiment, a variable that can be altered to suit the requirements of the imaging program. Far from compromising the sensitivity of the experiment, a suitable choice of pupil apodization can in fact enhance the signal-to-noise ratios of the Fourier measurements. In situations in which dense Fourier coverage is not required or in which instantaneous Fourier coverage is necessarily limited by other experimental considerations, the use of a slit mask is fully competitive with conventional filled-aperture speckle imaging, despite the large reduction in the detected flux. Indeed, it is this reduction of detected flux that is the most important advantage of pupil apodization at optical wavelengths. In situations in which detector performance is compromised by high flux rates (we have shown that these situations can occur in a large fraction of imaging experiments), pupil apodization is the method of choice for overcoming these detector limitations. Finally, we have shown that image reconstruction from the one-dimensional data obtained from slit pupils is straightforward and yields high-quality, reliable images. In terms of sensitivity and imaging fidelity, it provides the natural extension to nonredundant-mask methods, permitting high-resolution observations to be made at low light levels with good signal-to-noise ratio.

ACKNOWLEDGMENTS

We acknowledge the assistance of G. Neugebauer, S. Kulkarni, P. Gorham, K. Matthews, and A. Ghez, without whom the observations reported here would not have been possible. D. Buscher is employed by the Universities Space Research Association, 300 D Street, S.W., Washington, D.C. 20024, under contract with the Naval Research Laboratory/U.S. Naval Observatory Optical Interferometer Project. C. Haniff acknowledges financial support for this work from NATO, the UK Science and Engineering Research Council, and Christ's College, Cambridge, and thanks J. C. Dainty for the loan of computing hardware during the completion of this study.

*Current addresses: Mullard Radio Astronomy Observatory, Cavendish Laboratory, Madingley Road, Cambridge, CB3 0HE, England, and Institute of Astronomy, Madingley Road, Cambridge CB3 0HA, England.

REFERENCES

1. See, e.g., D. M. Alloin and J.-M. Mariotti, *Diffraction-Limited Imaging with Very Large Telescopes* (Kluwer, Dordrecht, The Netherlands, 1989), pp. 157–169 and 191–200.
2. G. R. Ayers, M. J. Northcott, and J. C. Dainty, "Knox–Thompson and triple correlation imaging through atmospheric turbulence," J. Opt. Soc. Am. A **5**, 963–985 (1988).
3. C. A. Haniff, C. D. Mackay, D. J. Titterington, D. Sivia, J. E. Baldwin, and P. J. Warner, "The first images from optical aperture synthesis," Nature (London) **328**, 694–696 (1988).
4. T. Nakajima, S. R. Kulkarni, P. W. Gorham, A. M. Ghez, G. Neugebauer, J. B. Oke, T. A. Prince, and A. C. S. Readhead, "Diffraction-limited imaging. II. Optical aperture synthesis imaging of two binary stars," Astron. J. **97**, 1510–1521 (1989).
5. J. G. Robertson, T. R. Bedding, R. G. Marson, P. R. Gillingham, R. H. Frater, J. D. O'Sullivan, and R. P. Norris, "High-resolution imaging by optical aperture synthesis: first results from the MAPPIT project," Proc. Astron. Soc. Aust. **9**, 162–163 (1991).
6. D. F. Buscher, C. A Haniff, J. E. Baldwin, and P. J. Warner, "Detection of a bright feature on the surface of Betelgeuse," M. Not. R. Astron. Soc. **245**, 7P–11P (1990).
7. C. A. Haniff, A. M. Ghez, P. W. Gorham, S. R. Kulkarni, K. Matthews, and G. Neugebauer, "Optical aperture synthetic imaging of the photosphere and molecular atmosphere of Mira," Astron. J. **103**, 1662–1667 (1992).
8. R. W. Wilson, J. E. Baldwin, D. F. Buscher, and P. J. Warner, "High-resolution imaging of Betelgeuse and Mira," M. Not. R. Astron. Soc. **257**, 369–376 (1992).
9. C. A. Haniff and D. F. Buscher, "Diffraction-limited imaging with partially redundant masks. I. Infrared imaging of bright objects," J. Opt. Soc. Am. A **9**, 203–218 (1992). (Paper 1).
10. C. Aime and F. Roddier, "One-dimensional stellar and solar speckle interferometry," Opt. Commun. **21**, 435–438 (1977).
11. S. Kadiri, C. Aime, and G. Ricort, "Speckle interférométrie à une dimension en astronomie: étude des fonctions de transfert instrument–atmosphère obtenues par analyze statistique de speckles stellaires fournis par un objectif rectangulaire," J. Opt. (Paris) **12**, 143–151 (1981).
12. C. Papalolios, P. Nisenson, and S. Ebstein, "Speckle imaging with the PAPA camera," Appl. Opt. **24**, 287–292 (1985).
13. P. R. Lawson, School of Physics, University of Sydney, Sydney, NSW 2006, Australia (personal communication, January 1993).
14. A. C. S. Readhead, T. Nakajima, T. J. Pearson, G. Neugebauer, J. B. Oke, and W. L. W. Sargent, "Diffraction-limited imaging with ground-based optical telescopes," Astron. J. **95**, 1278–1296 (1988).
15. F. Roddier, "Redundant versus nonredundant beam recombination in an aperture synthesis with coherent optical arrays," J. Opt. Soc. Am. A **4**, 1396–1401 (1987).
16. D. F. Buscher, "Getting the most out of C.O.A.S.T.," Ph.D. dissertation (Cambridge University, Cambridge, 1988).
17. J. W. Goodman and J. F. Belsher, "Fundamental limitations in linear invariant restoration of atmospherically degraded images," in *Imaging through the Atmosphere*, J. C. Wyant, ed., Proc. Soc. Photo-Opt. Instrum. Eng. **75**, 141–154 (1976).
18. J. C. Dainty and A. H. Greenaway, "Estimation of spatial power spectra in speckle interferometry," J. Opt. Soc. Am. **69**, 786–790 (1979).
19. S. N. Karbelkar, "Optimum weighting function in bispectral analysis in speckle interferometry: binary star parity detection," Astron. Astrophys. **238**, 485–493 (1990).
20. H. Bartelt, A. W. Lohmann, and B. Wirnitzer, "Phase and amplitude recovery from the bispectrum," Appl. Opt. **23**, 3121–3129 (1984).
21. R. G. Petrov, C. Aime, J. Borgnino, F. Martin, and G. Ricort, "16-m large slit aperture telescope for very high angular resolution astronomy," Proc. IAU Colloq. **79**, 295–308 (1984).
22. See, e.g., G. Weigelt, "Speckle interferometry, speckle holography, speckle spectroscopy and reconstruction of high-resolution images from ST data," in *Proceedings of the ESO Conference on the Scientific Importance of High Angular Resolution at Infrared and Optical Wavelengths*, M.-H.

Ulrich and K. Kjär, eds. (European Southern Observatory, Garching, Germany, 1981), pp. 95–114.
23. See, e.g., E. K. Hege, A. Eckart, and J. C. Christou, "The noise bias problem in optical speckle imaging: experience with a real detector," in *Instrumentation in Astronomy VI,* P. L. Crawford, ed., Proc. Soc. Photo-Opt. Instrum. Eng. **627,** 772–779 (1986).
24. K.-H. Hofmann, "Photon-counting speckle imaging: the photon-counting hole in triple correlation," J. Opt. Soc. Am. A **10,** 329–335 (1993).
25. P. W. Gorham, A. M. Ghez, S. R. Kulkarni, T. Nakajima, G. Neugebauer, J. B. Oke, and T. A. Prince, "Diffraction-limited imaging. III. 30mas closure phase imaging of six binary stars with the Hale 5 m telescope," Astron. J. **98,** 1783–1799 (1989).
26. F. Martin, A. Bijaoui, H. Touma, and C. Aime, "Astronomical image reconstruction via space slit aperture telescope," in *Infrared, Adaptive and Synthetic Aperture Optical Systems,* R. B. Johnson, W. L. Wolfe, and J. S. Fender, eds., Proc. Soc. Photo-Opt. Instrum. Eng. **643,** 189–193 (1986).
27. F. Martin, "Imagery in astronomy by inverse Radon transformation, using a rotating slit aperture telescope (SAT)," in *Inverse Problems in Optics,* E. R. Pike, ed., Proc. Soc. Photo-Opt. Instrum. Eng. **808,** 206–208 (1987).
28. F. Martin, H. Touma, A. Bijaoui, and C. Aime, "Reconstruction d'images en astronomie par utilisation d'un télescope à pupile fente," J. Opt. (Paris) **18,** 133–138 (1987).
29. T. J. Pearson and A. C. S. Readhead, "Image formation by self-calibration in radio astronomy," Ann. Rev. Astron. Astrophys. **22,** 97–130 (1984).
30. C. A. Haniff, D. F. Buscher, J. C. Christou, and S. T. Ridgway, "Synthetic aperture imaging at infrared wavelengths," M. Not. R. Astron. Soc. **241,** 51P–56P (1989).
31. C. A. Haniff, D. F. Buscher, J. C. Christou, and S. T. Ridgway, "Diffraction-limited imaging at IR wavelengths using aperture masks and fully-filled apertures," in *Amplitude and Intensity Spatial Interferometry,* J. B. Breckinridge, ed., Proc. Soc. Photo-Opt. Instrum. Eng **1237,** 259–271 (1990).